Journal of Quantitative Spectroscopy & Radiative Transfer 138 (2014) 36–49

Contents lists available at ScienceDirect

Journal of Quantitative Spectroscopy & Radiative Transfer

journal homepage: www.elsevier.com/locate/jqsrt

Estimation of the cirrus cloud scattering phase function from satellite observations

Chenxi Wang [a], Ping Yang [a,*], Andrew Dessler [a], Bryan A. Baum [b], Yongxiang Hu [c]

[a] Department of Atmospheric Sciences, Texas A&M University, College Station, TX 77843, USA
[b] Space Science and Engineering Center, University of Wisconsin-Madison, Madison, WI 53706, USA
[c] Climate Science Branch, NASA Langley Research Center, Hampton, Virginia 2368, USA

ARTICLE INFO

Article history:
Received 5 November 2013
Received in revised form
31 January 2014
Accepted 1 February 2014
Available online 7 February 2014

Keywords:
Thin cirrus clouds
Optical properties
Cloud phase function
Satellite observations

ABSTRACT

Optical and microphysical properties for optically thin ice clouds are retrieved from one year of collocated Aqua/MODIS and CALIPSO/CALIOP measurements in 2008. The values of optical thickness τ and effective particle size D_{eff} are inferred from MODIS measurements at three infrared (IR) bands located at 8.5, 11, and 12 μm in conjunction with collocated CALIOP cloud boundary altitudes and the MERRA atmospheric profile datasets. The τ values inferred from MODIS IR window measurements are insensitive to the pre-assumed particle and habit distributions. Based on near-IR measurements at 1.38 μm and the IR-based τ, a new method is developed to infer the scattering phase functions over both ocean and land. A comparison between theoretically calculated phase functions and the retrieved counterparts demonstrates that roughened solid columns provide the best match for cirrus clouds over ocean, whereas droxtals may exist in optically thin cirrus clouds. The best-fitted phase functions are generated using appropriate habit mixtures to match the inferred phase functions. The phase function resulting from a mixture of 55% severely roughened solid columns, 35% severely roughened droxtals, and 10% smooth aggregates almost perfectly matches the mean phase function value retrieved over ocean. The asymmetry factor based on the oceanic best-fitted phase functions is 0.778 at a wavelength of 0.65 μm. However, it is difficult to find an appropriate habit recipe to fit the inferred phase function over land. This may be caused by the relatively large uncertainties associated with τ retrievals over land. The retrieval of D_{eff} shows that optically thin cirrus clouds consist of smaller ice particles in comparison with optically thicker ice clouds. The mean D_{eff} values of optically thin ice clouds over land and ocean are 41 μm and 48 μm, respectively.

1. Introduction

Optically thin cirrus clouds, defined as those having optical thickness (τ) values less than 0.3, are frequently observed in the upper troposphere [1,2] and cover approximately 30% of the tropical region between 20°N–20°S [3]. In comparison with deep convection systems, optically thin cirrus clouds have relatively longer life cycles up to 2 days [4,5] and larger horizontal scales up to several hundred kilometers [6]. Meanwhile, the formation and maintenance of these clouds deplete water vapor by homogeneous freezing [7,8]. The study of these clouds has received a great deal of attention since 1980s due to their radiative importance [7,9]. Several studies show that optically thin cirrus clouds cause a positive radiative forcing at the top of the atmosphere (TOA). Optically thin cirrus modulates the global

* Corresponding author.
E-mail address: pyang@tamu.edu (Y. Hu).

http://dx.doi.org/10.1016/j.jqsrt.2014.02.001
0022-4073

energy budget primarily by emitting longwave (LW) radiation at a relatively low temperature [10,11] rather than reflecting shortwave (SW) energy. For example, using spaceborne lidar observations, Haladay and Stephens [3] demonstrated that the averaged TOA SW radiative forcing for optically thin cirrus clouds is less than $-2\,W\,m^{-2}$; but these clouds, located at relatively high altitudes, result in a significant decrease of the outgoing LW radiation of up to $20\,W\,m^{-2}$. Lee et al. [12] investigated the radiative properties of tropical optically thin cirrus clouds. They showed that the averaged TOA SW and LW forcings for all sky cases (i.e., including clear-sky and thin cirrus cases) are -1.7 and $2.7\,W\,m^{-2}$, respectively. The $1\,W\,m^{-2}$ net forcing in average is comparable with the effect of doubling CO_2 that leads to an approximate $4\,W\,m^{-2}$ radiative forcing [13].

It would be useful to have a more accurate description of optically thin cirrus optical and microphysical properties as well as single scattering properties necessary for radiative transfer simulations. The single scattering properties include the single scattering albedo, scattering/extinction efficiency, and scattering phase function, all of which are used to describe the patterns of energy absorbed or re-distributed by individual particles. Microphysical properties, such as the particle size distribution, habit distribution and the textures of ice particle surfaces (e.g., degrees of surface roughness, [14,15]), determine the single scattering properties of ice crystals and, consequently, the transfer field within cloud layers. However, knowledge of cloud microphysical properties is limited since such information is generally obtained from in situ measurements [16] or from cloud chambers. Note that in situ measurements may suffer from biases caused when large ice particles shatter at the inlet to the probes [17,18] and have spatial and temporal limitations. Ice particles developed in a cloud chamber also have limitations and may not capture the complexity of atmospheric particles.

For optically thin cloud, the use of traditional solar-reflectance bands to infer the τ and D_{eff} becomes problematic because the radiometric signals associated with cloud radiative properties are quite weak, especially over a reflective surface. Ackerman et al. [19] show some limitations in an analysis of the operational MODIS (Moderate Resolution Imaging Spectroradiometer; [20]) Collection 5 products [21]. Different from passive solar reflection observations, infrared (IR) and active lidar observations have advantages if the cloud is optically thin [4,22–26]. In the IR region, the relatively long incident wavelength is insensitive to the surface textures of individual particles. Satellite-based lidar is a powerful active instrument that provides backscattering signal profiles of atmospheric columns with high vertical resolution [27], and has inherent advantages in the detection of optically thin cirrus cloud layers.

To focus on optically thin cirrus clouds, a unique near-IR channel near the 1.38 μm water vapor absorption band is used. Strong absorption of water vapor generally prevents incident radiation from reaching the lower atmosphere and the surface. Therefore, measurements at this wavelength are sensitive to any cloud or scattering particle above the level where attenuation occurs [28,29] and is frequently used in the studies of optically thin cirrus clouds [30–33].

In this study, we infer optical thickness and effective particle size of optically thin cirrus clouds with 3 IR bands

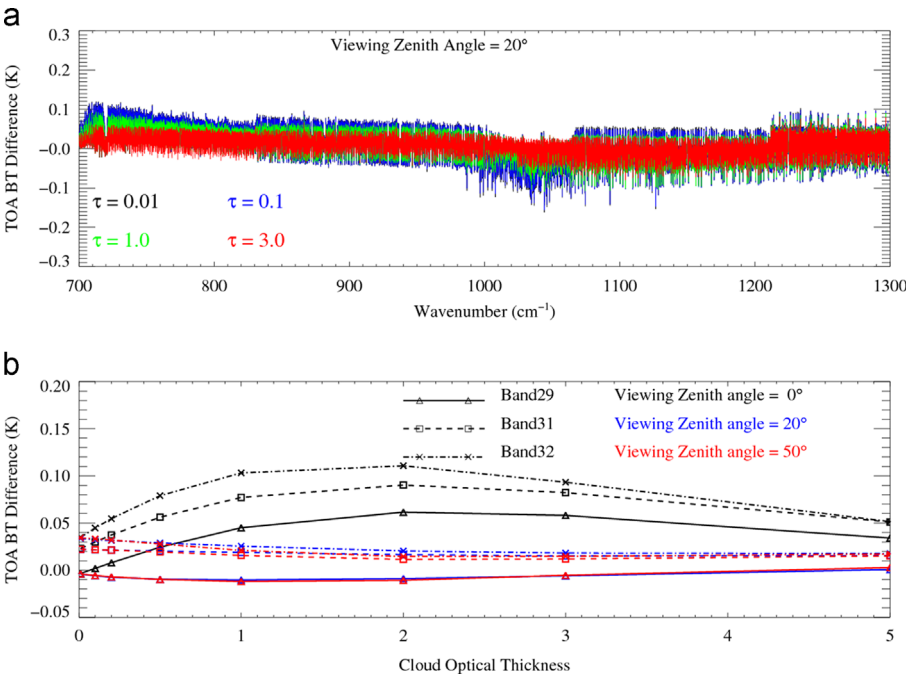

Fig. 1. TOA BT errors of the fast IR RTM in comparison with the 32-stream DISORT. A standard mid-latitude summer atmosphere is used to conduct the comparison. Panel (a): comparisons in a high-spectral resolution ($0.1\,cm^{-1}$) with viewing zenith angle 20°. Panel (b): simulations for three Aqua/MODIS IR bands (Band 29, 31, and 32) located near 8.5, 11, and 12 μm. Cloud D_{eff} values is 50 μm. The surface temperature is 299 K with albedo 0.05. The ice cloud top height is 10 km with physical thickness 1 km.

in global data. Additionally, a new method is developed to retrieve the cloud scattering phase function values in the side through backward scattering directions. We employ one year of *Aqua*/MODIS SW and IR observations in 2008 and collocated cloud mask products from the Cloud-Aerosol Lidar with Orthogonal Polarization (CALIOP) onboard the Cloud-Aerosol Lidar and Infrared Pathfinder Satellite Observations (CALIPSO, [27]).

This article is organized as follows. Sections 2 and 3 introduce the IR-based cloud optical thickness retrieval method, and the SW-based method to retrieve cloud microphysical properties, respectively. Results are presented in Section 4 and conclusions are given in Section 5.

2. Retrieval of cloud optical thickness and effective particle size

For clouds with an optical thickness less than approximately 5, IR window bands have inherent advantages in the retrieval of cloud optical thickness and effective particle size [34–40] since ice particles are strongly absorptive in this spectral region. In this study, we use three MODIS IR channels (8.5, 11, and 12 μm) and a fast IR radiative transfer model (RTM, [36,37]) to retrieve τ. The fast RTM simulates the TOA radiances in an IR spectral region (i.e., 700–1300 cm^{-1}) with satisfactory accuracy. Fig. 1a shows the comparisons between the fast model and the discrete ordinates radiative transfer model (DISORT, [41]) simulations with a high-spectral resolution (0.1 cm^{-1}). The channel-averaged errors in the three MODIS channels are generally smaller than 0.1 K in brightness temperatures (BTs) in comparison with DISORT (see Fig. 1b). The details of the IR fast RTM and corresponding retrieval algorithms are discussed in previous studies [36,37]. The retrieved cloud τ values are rescaled to the corresponding value at a visible wavelength (specifically, 0.65 μm) for convenience. The relation between τ_λ at an arbitrary wavelength λ and the corresponding τ at 0.65 μm is:

$$\tau_\lambda = \tau \frac{\langle Q_{ext,\lambda} \rangle}{\langle Q_{ext,vis} \rangle}, \quad (1)$$

where $\langle Q_{ext,\lambda} \rangle$ and $\langle Q_{ext,vis} \rangle$ represent bulk (averaged over the range of particle size and particle habits) extinction efficiencies at λ and 0.65 μm, respectively. It is a reasonable approximation to assume $\langle Q_{ext,vis} \rangle$ to be 2 since the typical size of ice particles is much larger than 0.65 μm. Ice particles have different absorption characteristics in the three MODIS IR channels. Information on particle sizes can be obtained by investigating the BT differences between the 8.5 and 11 (or 12) μm channels. Therefore, another parameter, D_{eff}, is also retrieved simultaneously with optical thickness.

In addition to the MODIS IR observations, the retrieval method uses surface temperature, surface emissivity, cloud boundary altitudes, and atmospheric profiles as input model parameters. The land surface temperature is extracted from the MODIS product [42]; the surface emissivities at three similar wavelengths (i.e., 8.6, 10.6, and 12 μm) are extracted from the product of the Infrared Imaging Radiometer (IIR) onboard the CALIPSO platform; the atmospheric profiles, such as the temperature, water vapor and ozone concentrations are from the Modern Era Retrospective-Analysis for Research and Applications (MERRA, [43]) data sets.

The cloud retrieval errors come from the satellite observations, model simulations, sensitivities of IR observations to cloud properties, and model input. Here we estimate the errors of τ and D_{eff} by introducing errors into different components of the IR-based retrieval. The measurement biases of the MODIS three IR channels are less than 0.1 K [44,45]. Brown and Minnett [46] reported a 0.35 K root mean square error (RMSE) of ocean surface temperature. The RMSE of land surface temperature is 1.0 K approximately [42,47]. RMSE errors of surface emissivities vary with surface type, and indicate that the ocean surface emissivity is accurate with RMSE error less than 0.01; while as the largest RMSE of surface emissivity (0.03) occurs in desert region [48]. Kennedy et al. [49] estimated the biases and RMSEs of the MERRA temperature and water vapor profiles. The MERRA temperature profiles have ± 0.3 K biases and RMSEs in the range between 1 and 2 K for lower atmosphere (pressure higher than 700 hPa). For high atmospheric layers, the MERRA temperature biases vary between -0.5 and 0.5 K with RMSE decreases to 1.0 K, approximately. The MERRA systematically underestimates water vapor concentration and have negative relative humidity biases in the lower atmosphere. The MERRA RMSEs of relative humidity are on the order of 10% in the entire atmosphere. More details about the error estimation of the MERRA temperature and water vapor profiles can be found in Fig. 1 in Kennedy et al. [49].

To conduct this error analysis, the 32-stream DISORT is used to provide the "true" TOA BTs in the three MODIS IR channels using a typical mid-latitude summer atmospheric

Table 1
Error sources introduced to conduct the error analysis for the IR-based retrieval.

Variable	Data source	Bias	RMSE
TOA BT	Aqua/MODIS L1B	0 K	0.1 K
Surface emissivity (ocean)	IIR/CALIPSO	0.0	0.01
Surface emissivity (land)	IIR/CALIPSO	0.0	0.03
Surface temperature (ocean)	Aqua/MODIS L2	0.0	0.5 K
Surface temperature (land)	Aqua/MODIS L2	0.0	1.0 K
Temperature profile	MERRA	−0.5–0.5 K	0.7–1.5 K
Water vapor profile	MERRA	−7 to 7%	5–18%

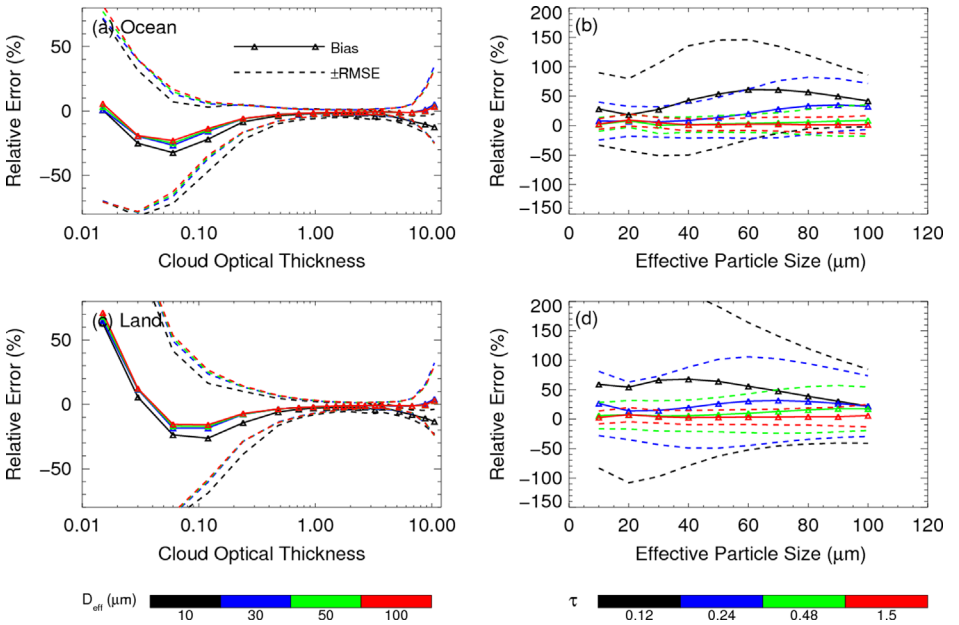

Fig. 2. Biases and RMSEs for ice cloud τ and D_{eff} retrievals calculated using 5000 perturbed atmospheric profiles. Errors from satellite observations, model simulations, and surface temperature and emissivity are also included. The standard mid-latitude summer profile is used for reference. The reference ocean surface temperature and emissivity are 299 K and 0.98, respectively; the land surface temperature and emissivity are 310 K and 0.9, respectively. Details of the error sources are listed in Table 1. Panels (a) and (c) show the error estimations for optical thickness retrievals over ocean and land, respectively. Panels (b) and (d) show the error estimations for D_{eff} retrievals over ocean and land, respectively.

profile [50], 20 cloud τ values from 0.015 to 10.5 and 10 D_{eff} values from 10 to 100 μm for reference. We also assume that errors from measurements, fast model simulations, and other input model parameters satisfy a normal distribution. Up to 5000 perturbed model inputs and TOA BTs (including both measurement and simulation errors) are employed to estimate retrieval errors over ocean and land. More details about the perturbations can be found in Table 1.

Fig. 2 shows the retrieval performance for different surface conditions. The accuracy of IR-based cloud retrievals can be significantly impacted by cloud optical thickness and surface type. Firstly, the bias and RMSE of retrieved τ increase rapidly as τ decreases from 0.1 to lower values; relatively large bias and RMSE of the D_{eff} retrieval also occur when τ is small. The MODIS IR window channel measurements are sensitive to optically thin cirrus cloud consisting of small particles, and therefore provide the highest sensitivity (i.e., the derivative of BT with respect to τ or D_{eff} is large). For the same ice cloud conditions, however, the information content can be extremely low since uncertainties from the lower atmosphere and the surface increase rapidly as the cloud becomes more optically thin. Secondly, the bias and RMSE increase as τ increases from 7 to 10. As optical thickness increases, particularly when τ is larger than 7, the impact of ancillary data uncertainties becomes less important on the retrieval accuracy. However, the retrieval accuracy also decreases because of the low information content caused by the near zero BT sensitivity to cloud properties. Furthermore, the retrieval biases may be amplified because the biases of temperature and water vapor concentration (as shown in Fig. 1 in [49]) have different signs and magnitudes at different vertical levels. There is an optimal range for IR τ retrievals, from 0.1–7. In this study, we focus on inferring cloud properties within this τ range, where the biases of cloud optical thickness retrieval are generally less than 20%. Similar error analyses are given by Kahn et al. [51] and Iwabuchi et al. [40].

3. Inference of ice habit information

The sensitivity in the shortwave infrared (SWIR: $0.75 < \lambda < 3$ μm) for the inference of ice habit and surface roughness is greater than in IR measurements because at SWIR wavelengths there is less absorption within ice particles. Cloud microphysical properties can be inferred by removing the optical thickness dependence from observations. In this section, an approach is developed to infer the phase function P for a SWIR wavelength of 1.38 μm. The phase function is not very sensitive to D_{eff} but is more sensitive to ice crystal habit. By comparing the inferred phase function with those from the various habits, it is possible to develop an ice crystal habit mixture that minimizes differences between the simulated and inferred phase functions, at least over the limited range of scattering angles available in the imager data. Note that in the following analysis, the intent is to focus on the optical properties of the habits rather than the microphysical properties, so the habit mixture may not resemble that of the general habit mixture in [14].

3.1. Physical principle

If an optically thin cirrus cloud layer exists in an atmospheric column, the SWIR bi-directional reflectivity

at wavelength λ is composed of several parts:

$$R_{obs,\lambda} = R_{c,\lambda} \times T_{two-way,\lambda} + b_\lambda + c_\lambda, \quad (2)$$

where $R_{obs,\lambda}$ is the satellite-observed reflectivity in this channel, $R_{c,\lambda}$ is the cirrus cloud reflectivity, $T_{two\text{-}way,\lambda}$ is the two-way transmissivity including the effect of gas absorption above the cloud layer, and b_λ and c_λ are reflectivities of the surface and gas molecules (i.e., the Rayleigh scattering) respectively. The two-way transmissivity is defined as follows:

$$T_{two-way,\lambda}(\tau_{g,\lambda}, \mu, -\mu_0) = \exp\left(-\frac{\tau_{g,\lambda}}{\mu}\right)\exp\left(\frac{\tau_{g,\lambda}}{\mu_0}\right), \quad (3)$$

where μ and μ_0 indicate the cosine values of the satellite viewing zenith angle and solar zenith angle, respectively. $\tau_{g,\lambda}$ is the gas optical thickness at wavelength λ. If cloud optical thickness is small, it is reasonable to derive the cloud scattering phase function based on the single-scattering approximation as follows:

$$P_\lambda(\Theta, M) \approx \frac{4R_{c,\lambda} \times (\mu+\mu_0)}{\omega_{o,\lambda}}\left[1-\exp\left(-\tau_{c,\lambda}\frac{\mu+\mu_0}{\mu\mu_0}\right)\right]^{-1}, \quad (4)$$

where P_λ is the scattering phase function, $\omega_{0,\lambda}$ is the single scattering albedo, $\tau_{c,\lambda}$ is the cloud optical thickness at wavelength λ, Θ is the scattering angle and M indicates cloud microphysical properties. However, the minimum cirrus cloud optical thickness that can be retrieved accurately is on the order of 0.1, at which point the accuracy of single scattering approximation decreases. Here we give a more general expression of Eq. (4) by introducing a multiple-scattering coefficient η_λ [52]:

$$P_\lambda(\Theta, M) \approx \frac{4\eta_\lambda R_{c,\lambda} \times (\mu+\mu_0)}{\omega_{o,\lambda}}\left[1-\exp\left(-\tau_{c,\lambda}\frac{\mu+\mu_0}{\mu\mu_0}\right)\right]^{-1}. \quad (5)$$

The multiple-scattering coefficient η_λ is defined as the ratio of single scattering to total reflectivity, which is a function of the incident-viewing geometry and cloud properties in the form

$$\eta_\lambda(\tau, M, \mu, \mu_0, \varphi) = \frac{Rs_{c,\lambda}}{R_{c,\lambda}}, \quad (6)$$

where φ indicates relative azimuthal angle, and $Rs_{c,\lambda}$ indicates the reflectivity contributed by single-scattering events. η_λ is close to 1 if cloud $\tau \ll 1$ and is lower than 1 for larger τ. η_λ is an important parameter in the derivation of the cloud scattering phase function. This is discussed in more detail in Section 3.2.

3.2. Derivation of cloud scattering phase function

To derive the scattering phase function P_λ using Eqs. (2)–(6), several variables (e.g., $T_{two\text{-}way,\lambda}$, b_λ, c_λ, $\omega_{0,\lambda}$, and η_λ) need to be calculated. In this study, we infer cloud P_λ from 1.38 μm measurements (MODIS band 26) for three reasons. Firstl, Rayleigh scattering is negligible in this spectral region [53]. Second, ice particles are weakly absorptive [54] and therefore the single scattering albedo $\omega_{0,\lambda}$ in Eq. (5) is close to 1 (see Fig. 3). Third, the surface contribution term b_λ is small in comparison with the cloud

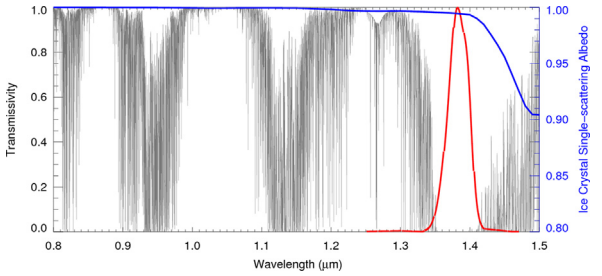

Fig. 3. The clear-sky transmissivity spectrum (gray) of a standard mid-latitude summer atmosphere calculated by using the LBLRTM. The blue curve is the ice crystals single scattering albedo. The red curve is the spectral response function of the MODIS Band26. (For interpretation of the references to color in this figure legend, the reader is referred to the web version of this article.)

reflectivity because of the strong water vapor absorption. Fig. 3 shows the clear-sky transmissivity spectrum of the typical mid-latitude summer atmosphere and the spectral response functions of the MODIS band 26. The transmissivity of the entire atmospheric column in the MODIS band 26 is approximately 0. The rigorous Line-By-Line Radiative Transfer Model (LBLRTM, [55]), the CALIOP cloud top altitude, and the MERRA atmospheric profiles are used to calculate the two-way transmissivity.

Eq. (6) implies that the multiple-scattering coefficient is determined by cloud optical and microphysical properties since both $Rs_{c,\lambda}$ and $R_{c,\lambda}$ are functions of τ and M. Therefore, a sensitivity study is implemented to investigate the relation between η_λ and cloud properties using two different bulk ice cloud microphysical models. The first microphysical model is currently employed in the MODIS Collection 5 ice cloud retrieval algorithm (hereafter referred to as Ice-C5, [56]) that was derived using more than 1100 ice particle size distributions obtained from tropical and mid-latitude ice clouds [17,57]. This model consists of 6 different ice particle habits (droxtals, plates, hollow and solid columns, solid bullet rosettes, and an aggregate of solid columns). The ice particles were assumed to have smooth surfaces, with the exception of the aggregate of solid columns for which moderate surface roughness was assumed. The second microphysical model is based on a generalized habit mixture (hereafter Ice-GHM; [14]) that adopted 3 new particle habits in addition to those previously listed for Ice-C5 (hollow bullet rosettes, small/large aggregate of plates) for a total of 9 habits.

In this model, all ice particles are assumed to have severely roughened surfaces where roughening of a particle surface consists of small tilted facets, as described in [58].

Fig. 4a shows multiple-scattering coefficient calculated using the Ice-C5 model $\eta_{Ice\text{-}C5,1.38}$ as a function of D_{eff}. This ratio is generally determined primarily by cloud optical thickness rather than the particle size. Fig. 4b shows the $\eta_{Ice\text{-}GHM,1.38}$-to-$\eta_{Ice\text{-}C5,1.38}$ ratio as a function of τ and D_{eff}. We find that the multiple-scattering coefficient is insensitive to the pre-assumed ice particle habits and surface roughness since the ratio is close to 1, especially in the D_{eff} region between 10 and 60 μm. For this reason, a pre-calculated lookup table (LUT) of $\eta_{1.38}$ is generated using the 128-stream DISORT, using the Ice_GHM habit mixture with

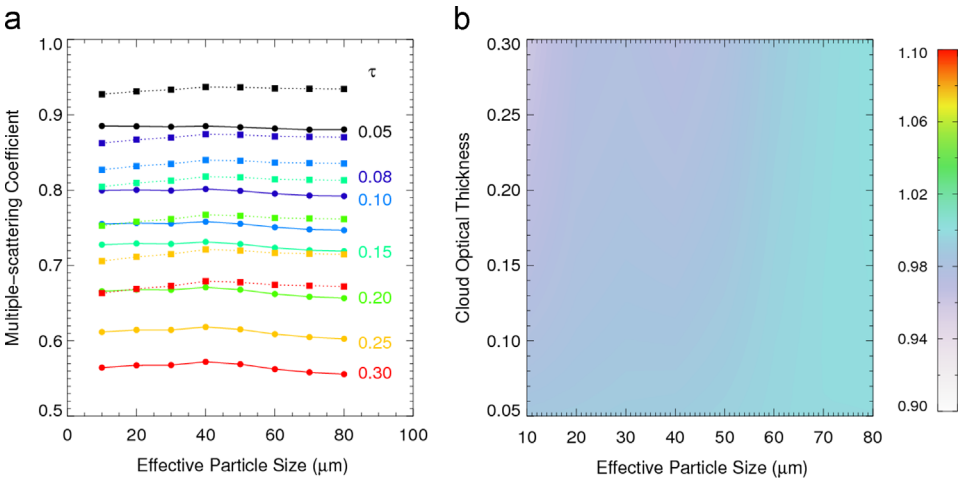

Fig. 4. Panel (a): the multiple-scattering coefficient ($\eta_{Ice\text{-}C5,1.38}$) as a function of D_{eff} calculated by using the Ice-C5 microphysical model. Solid curves: solar zenith angle, viewing zenith angle, and relative azimuthal angle are 21°, 63°, and 60°, respectively. The scattering angle is 105° approximately. Dotted curves: solar zenith angle, viewing zenith angle, and relative azimuthal angle are 28°, 50°, and 150°, respectively. The scattering angle is 152° approximately. Panel (b): the $\eta_{Ice\text{-}GHM,1.38}$-to-$\eta_{Ice\text{-}C5,1.38}$ ratio as a function of τ and D_{eff} with an scattering angle of approximately 105°.

a D_{eff} of 40 μm and including different incident-viewing angles, and optical thickness values. With the retrieved cloud τ and solar-satellite geometry, $\eta_{1.38}$ can be estimated.

The inferred thin cirrus cloud phase functions are compared with theoretical phase functions of bulk ice particles with one of the 9 ice particle habits and habit mixtures (e.g., the Ice-C5 and Ice-GHM). Cloud bulk scattering property is calculated by integrating corresponding single scattering properties over a wide range of sizes weighted by the gamma size distribution function and habit fraction. A combination of two numerical approaches is used to generate the database of ice particle single scattering properties. To be more specific, the Amsterdam discrete dipole approximation (ADDA, [59]) and the improved geometric optics method (the new IGOM, [60]) are employed to calculate the single scattering properties for small and large ice particles (see [61] for the technical details). In addition to the Ice-C5 and Ice-GHM, we also match inferred phase function values using a Monte Carlo method where the particle habits can be mixed without regard to whether it makes sense from a microphysical perspective. That is, any combination of the 9 habits and 2 degrees of surface roughness (only considering smooth and severely roughened) can be used if the radiative properties lead to a match between the simulated and inferred phase functions. In this Monte Carlo method, a random number R_1 between 0 and 1 is generated to represent the fraction of the first habit. The fraction of the nth habit with smooth or rough surface R_n ($2 < n < 18$) is limited to:

$$R_n \in \left[0, 1 - \sum_{i=1}^{n-1} R_i\right]. \tag{7}$$

Therefore, the fraction of the last habit is given by:

$$R_{18} = 1 - \sum_{i=1}^{17} R_i. \tag{8}$$

However, this strategy is not random since the last few habits always have extremely small fractions. Therefore, we randomly set the order of the habits every time before determining their fractions. A total number of 50 million habit mixtures are generated by using the Monte Carlo method to match the inferred scattering phase function at 30 scattering angles between 90° and 180°. The habit mixture with smallest cost function is chosen. The cost function is defined as follows:

$$\chi = \sqrt{\sum_{i=1}^{30} \left(\frac{\ln P_i - \ln P_{i,mixture}}{\ln \sigma_i}\right)^2} \tag{9}$$

where P and σ are the mean and standard deviation of inferred scattering phase function, $P_{mixture}$ is the phase function of a given habit mixture, i indicates the index of scattering angle. In the next section, we will discuss the retrieval results and the investigation of ice particle habits within thin cirrus clouds.

4. Results

Properties of optically thin cirrus clouds are investigated on the global scale using one full year of collocated *Aqua*/MODIS, Infrared Imaging Radiometer (IIR), and CALIOP/CALIPSO data in 2008. Three MODIS IR bands (e.g., 8.5, 11, and 12 μm) are used to retrieve cloud τ and D_{eff}. The MODIS SWIR band at 1.38 μm is used to derive the cloud bulk scattering phase function. MODIS pixels containing multi-layered clouds, water phase clouds, or mixed phase clouds are eliminated using the CALIOP cloud products. Only CALIOP-detected ice phase clouds [62] with cloud base altitudes higher than 8 km are used to retrieve cloud τ and D_{eff}. Furthermore, optically thin cirrus samples with τ values (retrieved using the IR-method) in the range between 0.1 and 0.3 are used to infer cloud scattering phase functions. Note that the retrieved phase function is limited to optically thin cirrus clouds during the daytime since MODIS SWIR observations are required.

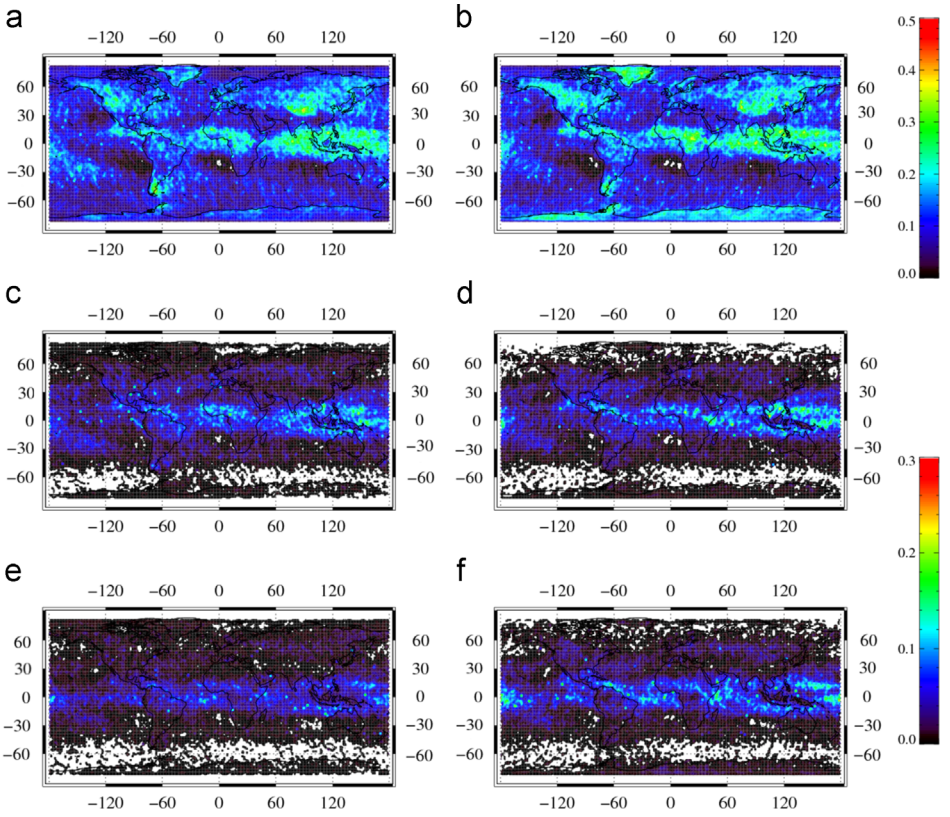

Fig. 5. CALIOP detected daytime (left column) and nighttime (right column) frequencies of single layer ice clouds, optically thin cirrus clouds (i.e., $0.03 < \tau_{CALIOP} < 0.3$), and subvisible cirrus ($\tau_{CALIOP} < 0.03$) in 2008. (a) Ice cloud Frequency (Daytime), (b) Ice cloud Frequency (Nighttime), (c) Thin Cirrus Frequency (Daytime), (d) Thin Cirrus Frequency (Nighttime), (e) Subvisible Cirrus Frequency (Daytime) and (f) Subvisible Cirrus Frequency (Night time).

4.1. Overview

Fig. 5 shows the geographical distributions of CALIPSO detected ice clouds [62], optically thin cirrus clouds (CALIOP $0.03 < \tau < 0.3$ [27]), and subvisible cirrus clouds (CALIOP $\tau < 0.03$) for daytime and nighttime, respectively. Note that in this study the analysis is limited to CALIOP detected single-layered cloud cases where the optically thin cirrus clouds and subvisible cirrus clouds have cloud bases higher than 8 km. For optically thick ice clouds (e.g. $\tau > 3$), the CALIOP signal attenuates rapidly and cannot detect lower-level clouds. Therefore, the collocated Cloud-sat product [63] is used to eliminate multi-layered cases. In comparison with the frequency of all ice clouds found, the optically thin cirrus cloud primarily resides in the tropics. The high frequency regions are found in the western Pacific, Africa, and across South America, consistent with previous studies. The daytime and nighttime data indicate similar frequency patterns for both all ice clouds and optically thin cirrus cloud. However, more sub-visible cirrus clouds are found by CALIOP during the nighttime, as expected since the signal-to-noise ratio is quite high during the daytime. During the daytime, the lidar-based cloud detection algorithm may be influenced by reflected solar radiance. The CALIOP cloud detection algorithm needs to increase a threshold of cloud-to-gas molecule scattering ratio to reduce the solar impact. A fraction of sub-visible cloud signals are also eliminated because of the increase of the threshold value [64,65]. Similar results of CALIOP detected ice cloud frequencies are reported by Sassen et al. [66].

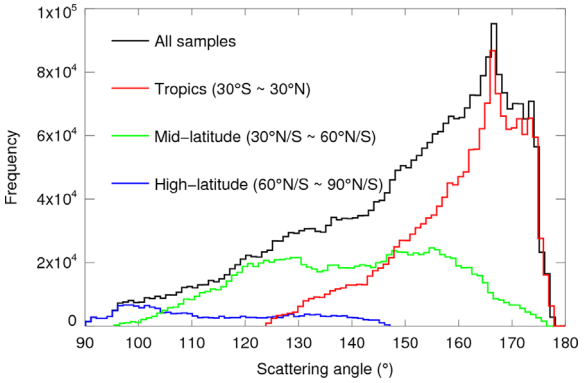

Fig. 6. Scattering angle frequencies for global, low- (30°S to 30°N), mid- (30°N/S to 60°N/S), and high-latitude (60°N/S to 90°N/S) optically thin cirrus samples.

A scattering phase function at only one scattering angle can be retrieved from an optically thin cirrus sample using the collocated MODIS and CALIOP observations. Therefore, a range of cloud scattering phase function can only be retrieved using a large amount of observations with different locations and times. Fig. 6 shows the scattering

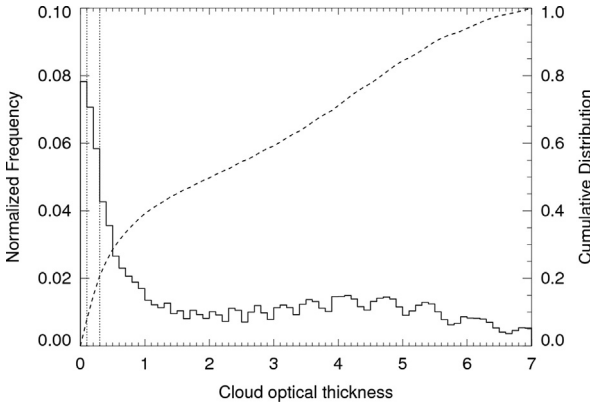

Fig. 7. Normalized frequency (solid) and cumulative distribution (dashed curve) of retrieved ice cloud τ (at visible wavelength) using IR-based method. The two dotted vertical lines represent τ=0.1 and 0.3, respectively.

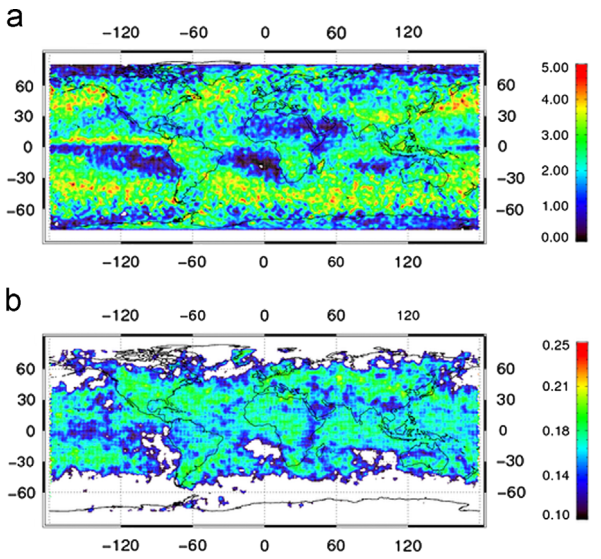

Fig. 8. Annual averaged IR-based τ distribution patterns of (a) ice clouds, and (b) optically thin cirrus clouds ($0.1 < \tau < 0.3$).

angle frequencies for global, low, mid, and high latitude optically thin cirrus clouds. A large fraction of the optically thin cirrus cloud samples have scattering angles higher than 120° because: (1) more than 85% of optically thin cirrus cloud samples occur in the tropics with relatively small solar zenith angles, and (2) the CALIOP track varies little over the MODIS swath, limiting comparison with MODIS observations to a narrow range of viewing zenith angles (e.g., smaller than 20°). Collocation samples with scattering angles less than 110° are located primarily at very high latitudes in both hemispheres.

4.2. Cirrus optical properties

MODIS IR measurements are used to investigate cirrus optical properties for both daytime and nighttime cirrus clouds, again limited to ice phase clouds having base

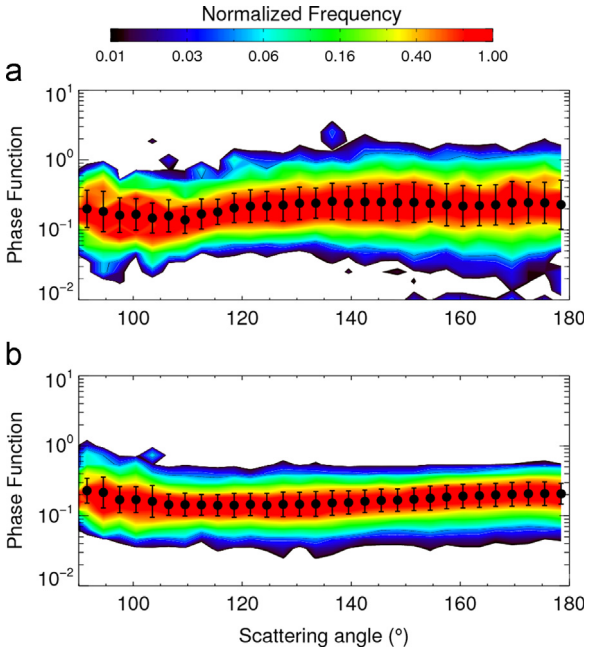

Fig. 9. Scattering plot of inferred optically thin cirrus cloud phase function over land (a) and over ocean (b). Black circles represent the averaged phase functions. Error bars indicate corresponding standard deviations. The frequency is scaled by dividing the largest frequency in each scattering angle bin.

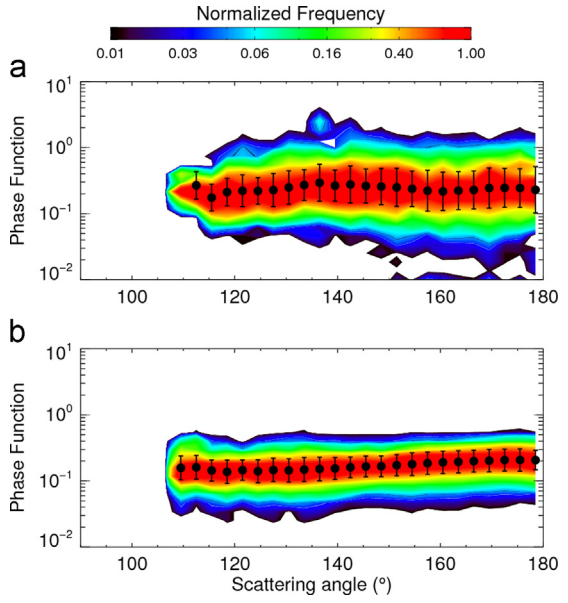

Fig. 10. Same as Fig. 9, but samples in low-latitude region (45°S–45°N) are plotted. The Sahara Desert region (i.e., 5°N–35°N, 20°W and 35°E) is removed to reduce the impacts from the surface.

altitudes higher than 8 km. Fig. 7 shows the normalized and cumulative τ frequencies. About 20% of the cirrus samples have τ smaller than 0.3. Given the error analysis discussed in Section 2, we focus on ice clouds with retrieved τ values between 0.1 and 7. Additionally, optically thin cirrus clouds (about 14% of all samples, see the vertical dotted lines in

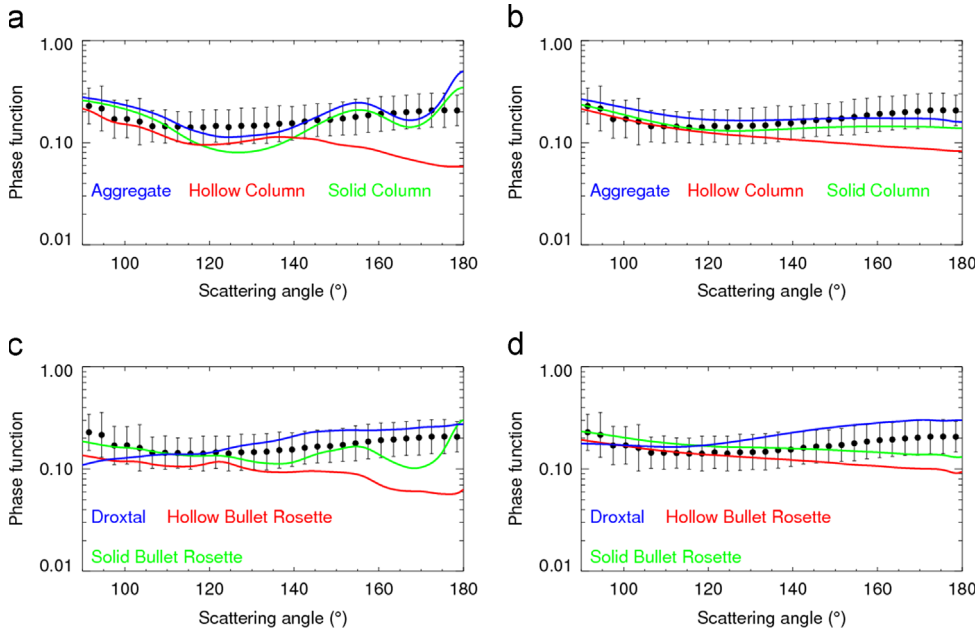

Fig. 11. Comparisons between inferred scattering phase function of oceanic thin cirrus clouds (black dots as shown in Fig. 9b) and scattering phase functions of ice crystals with ideal habits. (a-c): Smooth particles and (b-d): Rough particles.

Fig. 7) with retrieved τ values between 0.1 and 0.3 are used to investigate the inference of the scattering phase function. The global annually-averaged τ distributions for single ice cloud layer samples (with retrieved $0.1 < \tau < 7$) and for optically thin cirrus cloud samples ($0.1 < \tau < 0.3$) are shown in Fig. 8. For all ice cloud samples, the averaged τ displays a similar geographical distribution pattern as shown previously (see Fig. 5). However, insignificant spatial variations can be found from the geographical distribution of τ for optically thin cirrus clouds, suggesting that the τ values of optically thin cirrus clouds are essentially independent of the frequency of occurrences.

4.3. Cirrus microphysical properties

Based on the IR-based cloud optical thickness, the optically thin cirrus cloud phase functions over land and ocean are shown in Fig. 9a and b, respectively. The mean values of the phase functions (circles) and corresponding standard deviations (vertical bars) are shown. Although multiple scattering events, together with averaging a large number of phase function values within a narrow scattering angle range, tend to smooth out the inferred scattering phase function, we can still infer some features via this investigation. For example, relatively strong oscillations can be found in the averaged land-based phase function in the scattering angle range between 100° and 180°. Additionally, the standard deviations of the land phase functions are much larger than their oceanic counterparts. Different from the land phase function, the averaged oceanic phase function exhibits a slight increase at scattering angles larger than 120°. The larger uncertainties from the inferred phase functions over land may be a result of two factors: fewer cirrus samples are collected over land and there are larger uncertainties of land surface temperature and emissivity. The 1.38 μm reflectivity may be impacted by the surface if the amount of total precipitable water in the column is low (e.g., in high-latitude regions) or if the surface is strongly reflective (desert regions). To reduce these potential uncertainties, the data are filtered using mid- and low-latitude cloudy samples only between 45°N and 45°S. Furthermore, cirrus pixels over the Sahara Desert region (i.e., 5°N–35°N, 20°W and 35°E) are also removed. The filtered scattering phase functions are shown in Fig. 10. Samples with low scattering angles ($\Theta < 110°$) are already removed since these are noted to occur most often at higher latitudes. Even with this filtering, no significant change over land can be found in either of the averaged phase functions and their corresponding standard deviations.

We compare the inferred cloud phase functions with theoretical ice particle phase functions with uniform habits and degrees of surface roughness, as shown in Figs. 11 and 12. In the two figures, the left and right columns show the theoretical phase functions for smooth and roughened particles, respectively. In comparison with smooth particles, the phase functions of roughened particles seem to be quite similar to the inferred oceanic phase function, suggesting that roughened particles (especially solid columns and column aggregates) may dominate optically thin cirrus clouds over ocean. Baum et al. [14] show that in synoptic cirrus clouds, water droplets that have multiple nucleation events upon freezing are likely to grow as poly-crystals. However, it is found that the phase function of droxtals generally captures the gradual increment in side through backward directions of the inferred oceanic phase function. Baum et al. [14] reported that droxtals might exist near the top of synoptic clouds in

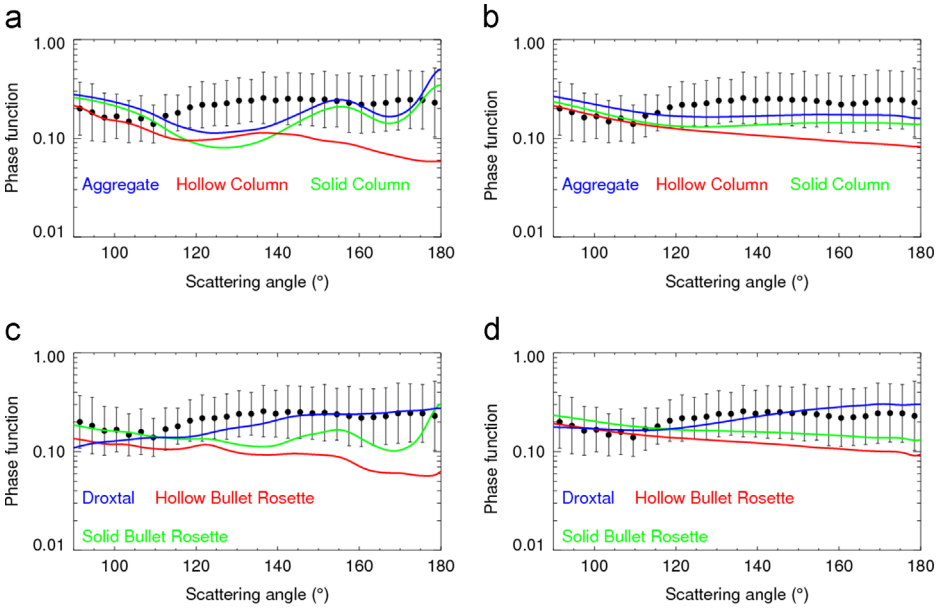

Fig. 12. Same as Fig. 11, but for comparisons between theoretical scattering phase functions and inferred scattering phase function of thin cirrus clouds over land. (a-c): Smooth particles and (b-d): Rough particles.

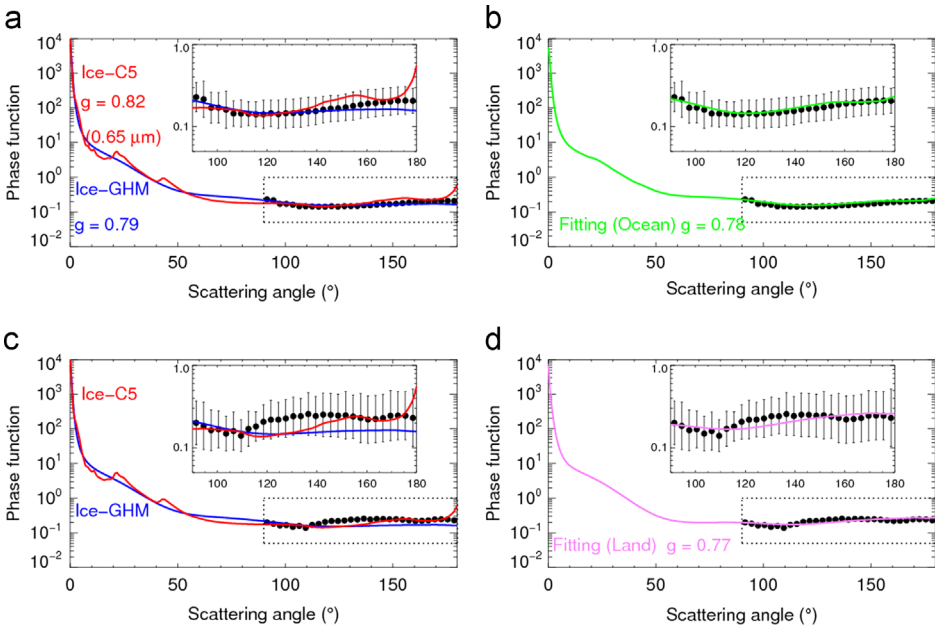

Fig. 13. Left column: comparisons between the theoretical phase functions calculated using habit mixtures (Ice-C5 and Ice-GHM) and the inferred phase functions over ocean and land. Right column: comparisons between the best-fitting phase functions and inferred phase functions over ocean and land.

the upper troposphere with ambient temperature between −60 and −40 °C.

Fig. 13 compares the inferred cloud phase functions and the theoretical phase functions calculated using habit mixtures. Two ice cloud microphysical models (i.e., Ice-C5 and Ice-GHM) mentioned in Section 3 are used to conduct the comparisons. The assumption of smooth particles in the Ice-C5 model leads to relatively strong phase function oscillations and strong backward scattering. The phase function of Ice-GHM captures the major features of the inferred phase function, suggesting that the assumption of severely roughened particles is sufficient to simulate thin cirrus clouds.

The best-fitted scattering functions for oceanic and land optically thin cirrus clouds are generated by using the Monte Carlo method and are shown in the right column of Fig. 13. In the Monte Carlo method, the effective diameter is assumed to be 40 μm. This is because the

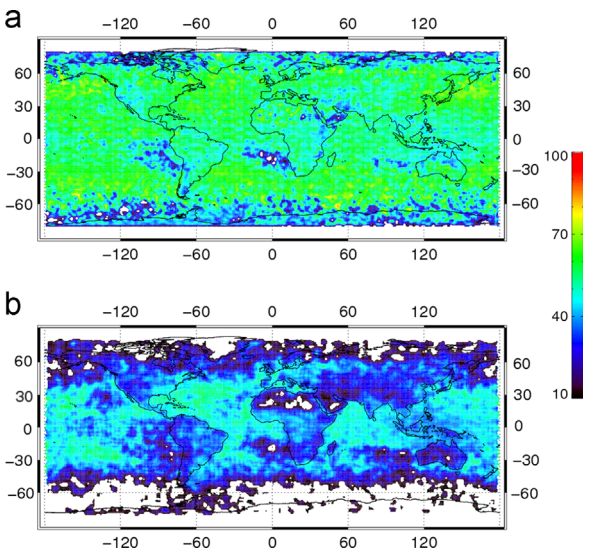

Fig. 14. Annual averaged IR-based D_{eff} distribution patterns of (a) ice clouds, and (b) optically thin cirrus clouds ($0.1 < \tau < 0.3$).

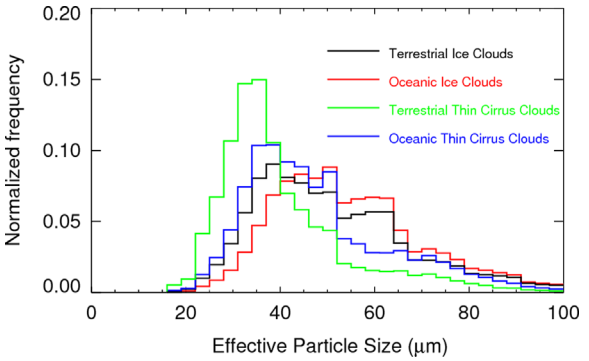

Fig. 15. Normalized Frequencies of D_{eff} for terrestrial ice clouds (black), oceanic ice clouds (red), terrestrial thin cirrus clouds (green), and oceanic thin cirrus clouds (blue). (For interpretation of the references to color in this figure legend, the reader is referred to the web version of this article.)

Table 2
Annual means of global, oceanic, and terrestrial cloud D_{eff} for ice clouds and optically thin cirrus clouds.

Cloud properties (global annual mean)	D_{eff} (μm)
Ice cloud	
Global	53
Oceanic	54
Terrestrial	51
Optically thin cirrus	
Global	47
Oceanic	48
Terrestrial	41

variation of a phase function with a change of D_{eff} can be ignored in comparison with the standard deviation of inferred phase function. The best-fitted oceanic scattering phase function almost perfectly matches the inferred one. This approach suggests that the use of 55% severely roughened solid columns, 35% severely roughened droxtals, and 10% smooth aggregates is adequate to represent the ice particle optical properties within oceanic thin cirrus clouds over this limited scattering angle range.

For clouds over land, the best-fitted phase function does not match the inferred phase function because none of the idealized ice particle habits reproduces a similar phase function. For scattering angles larger than 120°, almost all of the habits have a lower value in the scattering phase function in comparison with the inferred one, except the droxtal. For this reason, the best-fitted habit mixture consists of 76% severely roughened droxtals and 24% severely roughened solid bullet rosettes. Generally speaking, more uncertainties are associated with the inferred phase function over land. More studies are required to investigate the difference the oceanic and terrestrial thin cirrus clouds. With a D_{eff} of 40 μm, the asymmetry factors for the two best-fitted phase functions over ocean and over land 0.785 and 0.774 at 1.38 μm, and 0.778 and 0.769 at 0.65 μm. The Ice-C5 and Ice-GHM have relatively larger asymmetry factors (0.814 and 0.797 at 1.38 μm, and 0.818 and 0.790 at 0.65 μm).

The two best-fitted ice cloud microphysical models, together with the MODIS IR observations, are used to retrieve D_{eff} for cirrus clouds over ocean and land, respectively. Here the best-fitted habits mixtures are used to retrieve ice cloud properties with τ values larger than 0.3, although they are derived from optically thin cirrus clouds. This may not be representative of thicker ice clouds. The geographical distributions of annual averaged D_{eff} for ice clouds and optically thin cirrus clouds are shown in the two panels of Fig. 14, respectively. It is interesting to find that the ice cloud D_{eff} values are systematically larger than the optically thin cirrus clouds. Additionally, it seems that the oceanic optically thin cirrus clouds consist of relatively larger ice particles than their land counterparts. As shown in Fig. 15, the averaged D_{eff} values for ice clouds and optically thin cirrus clouds over land are 51 μm and 41 μm, respectively. However, the mean D_{eff} values for all ice clouds and optically thin ice clouds over ocean are 54 μm and 48 μm (see Table 2). King et al. [67] reported the climatology for ice cloud properties using the MODIS Collection 5 optical thickness and effective particle size. Some discrepancies can be found in comparison with this study. However, the MODIS operational cloud retrieval that uses a combination of two solar reflectance channels is much more sensitive to optically thick (e.g., $\tau > 5$) clouds rather than optically thin cirrus cloud ($0.1 < \tau < 0.3$). The optically thick ice clouds with τ larger than 7 are beyond the IR retrievable range and therefore are eliminated in this study. According to the error analysis mentioned in Section 2, the IR-based retrieval is likely to overestimate D_{eff} by a factor of 1.1–1.5 for oceanic optically thin cloud and a factor of 1.3–1.6 for optically thin cloud over land. In the future, an optimal estimation-based method [68] could be used to understand retrieval uncertainties at the pixel-level.

5. Conclusions

In this study, a new method using a combination of satellite IR and SW observations is developed to infer

optical and microphysical properties of optically thin cirrus cloud on a global scale. Three MODIS IR channel observations, together with the collocated CALIOP cloud boundary altitudes and atmospheric profiles from the MERRA data, are used to infer cloud optical thickness and effective particle size. The IR observations are insensitive to the ice particle size and habit distributions, facilitating the retrieval of τ without accurate knowledge of cloud microphysical properties and possible vertical inhomogeneity of ice crystal habit [69]. The IR-based retrieval method is based on a fast and accurate RTM. The errors of τ and D_{eff} retrievals are estimated. To reduce the impacts from cloud retrieval uncertainties, only optically thin cirrus cloud with retrieved τ values larger than 0.1 are used to infer cloud microphysical properties. The SWIR measurements at 1.38 μm have some sensitivity to particle habits and the degree of surface roughness. Therefore, the MODIS SWIR 1.38 μm band is used to infer cloud scattering phase functions statistically. The 1.38 μm channel is used to reduce the impact from surface reflection and highlight thin cirrus clouds in the upper troposphere.

From the inferred cloud optical properties we find that the geographical pattern of τ distribution for all ice clouds is similar to their occurrence frequency. However, for optically thin cirrus clouds, the averaged τ distribution is essentially independent of with their frequency of occurrence. Furthermore, slight differences in the optical thickness are found between ocean and land. By investigating effective particle diameter (to be consistent with rest of manuscript), we find that the optically thin cirrus clouds are composed of relatively small ice particles in comparison with the optically thick ice clouds. The global mean D_{eff} values of all ice cloud and optically thin cirrus samples are 53 and 47 μm, respectively. Meanwhile, the averaged D_{eff} values of the two different ice cloud types exhibit strong spatial dependence, that is, the D_{eff} values of oceanic ice clouds are systematically larger than their terrestrial counterparts. Future studies focusing on the differences between oceanic and terrestrial thin cirrus clouds are necessary. Investigation of the inferred and theoretical phase functions suggests that the optical properties of optically thin cirrus clouds over ocean are approximated well by a combination of roughened solid columns, droxtals, and smooth column aggregates.

An optimal mixture of ice particle habits may be suggested using the Monte Carlo method. It shows that the phase function from an ensemble of 55% severely roughened solid columns, 35% severely roughened droxtals, and 10% smooth aggregates almost perfectly matches the inferred oceanic scattering phase function. The inferred scattering phase function over land indicates strong oscillations in the side through backward scattering directions (scattering angle between 110° and 180°). Based on minimizing the inferred and simulated phase function differences, the optimal mixture of the ice particle habits for terrestrial thin cirrus clouds obtained from the Monte Carlo method is 76% severely roughened droxtals and 24% severely roughened solid bullet rosettes. However, it is difficult to use current theoretical phase functions to match the terrestrial cirrus phase function. In comparison with oceans, analysis of ice particle habits in thin cirrus clouds over land is much more difficult due to the large uncertainties associated with surface temperature and emissivity, which impact the IR-based τ retrieval.

Acknowledgments

This study is supported by NASA grants NNX10AM27G, NNX11AK37G, and NNX11AF40G (the associated subcontract to Texas A&M University through the University of Wisconsin-Madison, 301K630). Bryan Baum and Ping Yang thank Drs. Ramesh Kakar and Hal Maring for their encouragement and support over the years.

References

[1] Prabhakara C, Kratz DP, Yoo JM, Dalu G, Vernekar A. Optically thin cirrus clouds: radiative impact on the warm pool. J Quant Spectrosc Radiat Transfer 1993;49:467–83.
[2] Wang P-H, McCormick MP, Poole LR, Chu WP, Yue GK, Kent GS, et al. Tropical high cloud characteristics derived from SAGE II extinction measurements. Atmos Res 1994;34:53–83.
[3] Haladay T, Stephens G. Characteristics of tropical thin cirrus clouds deduced from joint CloudSat and CALIPSO observations. J Geophys Res 2009;114:D00A25.
[4] Winker DM, Trepte CR. Laminar cirrus observed near the tropical tropopause by LITE. Geophys Res Lett 1998;25:3351–4.
[5] Luo Z, Rossow WB. Characterizing tropical cirrus life cycle, evolution, and interaction with upper-tropospheric water vapor using Lagrangian trajectory analysis of satellite observations. J Clim 2004;17:4541–63.
[6] Heymsfield AJ, McFarquhar GM. Mid-latitude and tropical cirrus: microphysical properties. In: Lynch DK, Sassen K, Starr DO, Stephens D, editors. Cirrus, New York: Oxford University Press; 2002.
[7] Jensen EJ, Toon OB, Selkirk HB, Spinhirne JD, Schoeberl MR. On the formation and persistence of subvisible cirrus clouds near the tropical tropopause. J Geophys Res 1996;101:21361–75.
[8] Steinwagner J, Fueglistaler S, Stiller G, von Clarmann T, Kiefer M, Borsboom P-P, et al. Tropical dehydration processes constrained by the seasonality of stratospheric deuterated water. Nat Geosci 2010;3:262–6.
[9] McFarquhar GM, Heymsfield AJ, Spinhirne J, Hart B. Thin and subvisual tropopause tropical cirrus: observations and radiative impacts. J Atmos Sci 2000;57:1841–53.
[10] Liou K-N. Influence of cirrus clouds on weather and climate processes: a global perspective. Mon Weather Rev 1986;114:1167–99.
[11] Rosenfield JE, Considine DB, Schoeberl MR, Browell EV. The impact of subvisible cirrus clouds near the tropical tropopause on stratospheric water vapor. Geophys Res Lett 1998;25:1883–6.
[12] Lee J, Yang P, Dessler AE, Gao B-C, Platnick S. Distribution and radiative forcing of tropical thin cirrus clouds. J Atmos Sci 2009;66:3721–31.
[13] Ramanathan V, Callis L, Cess R, Hansen J, Isaksen I, Kuhn W, et al. Climate-chemical interactions and effects of changing atmospheric trace gases. Rev Geophys 1987;25:1441–82.
[14] Baum BA, Yang P, Heymsfield AJ, Schmitt CG, Xie Y, Bansemer A, et al. Improvements in shortwave bulk scattering and absorption models for the remote sensing of ice clouds. J Appl Meteorol Climatol 2011;50:1037–56.
[15] Neshyba SP, Lowen B, Benning M, Lawson A, Rowe PM. Roughness metrics of prismatic facets of ice. J Geophys Res 2013;118:3309–18.
[16] Heymsfield A, Winker D, Avery M, Vaughan M, Diskin G, Deng M, et al. Relationships between ice water content and volume extinction coefficient from in situ observations for temperatures from 0 °C to −86 °C: implications for spaceborne lidar retrievals. J Appl Meteorol Climatol 2014;. http://dx.doi.org/10.1175/JAMC-D-13-087.1 [in press].
[17] Heymsfield AJ, Bansemer A, Schmitt C, Twohy C, Poellot MR. Effective ice particle densities derived from aircraft data. J Atmos Sci 2004;61:982–1003.
[18] Field PR, Heymsfield AJ, Bansemer A. Shattering and particle interarrival rimes measured by optical array probes in ice clouds. J Atmos Ocean Technol 2006;23:1357–71.

[19] Ackerman SA, Holz RE, Frey R, Eloranta EW, Maddux BC, McGill M. Cloud detection with MODIS. Part II: validation. J Atmos Ocean Technol 2008;25:1073–86.
[20] King M.D., Tsay S-C, Platnick SE, Wang M, Liou K-N. Cloud retrieval algorithms for MODIS: optical thickness, effective particle radius, and thermodynamic phase. MODIS Algorithm Theoretical Basis Document, No. ATBD-MOD; 1997; 5.
[21] Platnick S, King MD, Ackerman SA, Menzel WP, Baum BA, Riedi JC, et al. The MODIS cloud products: algorithms and examples from Terra. IEEE Trans Geosci Remote Sens 2003;41:459–73.
[22] Wylie DP, Menzel WP. Eight years of high cloud statistics using HIRS. J Clim 1999;12:170–84.
[23] Baran AJ. On the scattering and absorption properties of cirrus cloud. J Quant Spectrosc Radiat Transfer 2004;89:17–36.
[24] Baran AJ, Francis PN. On the radiative properties of cirrus cloud at solar and thermal wavelengths: a test of model consistency using high-resolution airborne radiance measurements. Q J R Meteorol Soc 2004;130:763–78.
[25] Stubenrauch CJ, Chédin A, Rädel G, Scott NA, Serrar S. Cloud properties and rheir seasonal and diurnal variability from TOVS Path-B. J Clim 2006;19:5531–53.
[26] Reichardt J, Reichardt S, Yang P, McGee TJ. Retrieval of polar stratospheric cloud microphysical properties from lidar measurements: dependence on particle shape assumptions. J Geophys Res 2002;107:8282.
[27] Winker DM, Vaughan MA, Omar A, Hu Y, Powell KA, Liu Z, et al. Overview of the CALIPSO Mission and CALIOP data processing algorithms. J Atmos Ocean Technol 2009;26:2310–23.
[28] Gao B-C, Yang P, Wei H, Li R-R, Wiscombe WJ. An algorithm using visible and 1.38-μm channels to retrieve cirrus cloud reflectances from aircraft and satellite data. IEEE Trans Geosci Remote Sens 2002;40:1659–68.
[29] Gao B-C, Kaufman YJ, Han W, Wiscombe WJ. Corection of thin cirrus path radiances in the 0.4–1.0 μm spectral region using the sensitive 1.375 μm cirrus detecting channel. J Geophys Res 1998;103: 32169–76.
[30] Dessler AE, Yang P. The distribution of tropical thin cirrus clouds inferred from Terra MODIS data. J Clim 2003;16:1241–7.
[31] Meyer K, Yang P, Gao B-C. Optical thickness of tropical cirrus clouds derived from the MODIS 0.66 and 1.375-micron channels. IEEE Trans Geosci Remote Sens 2004;42:833–41.
[32] Meyer K, Platnick S. Utilizing the MODIS 1.38 μm channel for cirrus cloud optical thickness retrievals: algorithm and retrieval uncertainties. J Geophys Res 2010;115:D24209.
[33] Wang C, Ding S, Yang P, Baum B, Dessler AE. A new approach to retrieving cirrus cloud height with a combination of MODIS 1.24- and 1.38-μm channels. Geophys Res Lett 2012;39:L24806.
[34] Inoue T. On the temperature and effective emissivity determination of semi-transparent cirrus clouds by bi-spectral measurements in the 10 μm window region. J Meteorol Soc Jpn 1985;63:88–99.
[35] Wei H, Yang P, Li J, Baum BA, Huang HL, Platnick S, et al. Retrieval of semitransparent ice cloud optical thickness from atmospheric infrared sounder (AIRS) measurements. IEEE Trans Geosci Remote Sens 2004;42:2254–67.
[36] Wang C, Yang P, Baum BA, Platnick S, Heidinger AK, Hu Y, et al. Retrieval of ice cloud optical thickness and effective particle size using a fast infrared radiative transfer model. J Appl Meteorol Climatol 2011;50:2283–97.
[37] Wang C, Yang P, Platnick S, Heidinger AK, Baum BA, Greenwald T, et al. Retrieval of ice cloud properties from AIRS and MODIS observations based on a fast high-spectral-resolution radiative transfer model. J Appl Meteorol Climatol 2013;52:710–26.
[38] Garnier A, Pelon J, Dubuisson P, Faivre M, Chomette O, Pascal N, et al. Retrieval of cloud properties using CALIPSO Imaging Infrared Radiometer. Part I: effective emissivity and optical depth. J Appl Meteorol Climatol 2012;51:1407–25.
[39] Garnier A, Pelon J, Dubuisson P, Yang P, Faivre M, Chomette O, et al. Retrieval of cloud properties using CALIPSO Imaging Infrared Radiometer. Part II: effective diameter and ice water path. J Appl Meteorol Climatol 2013;52:2582–99.
[40] Iwabuchi H, Yamada S, Katagiri S, Yang P, Okamoto H. Radiative and microphysical properties of cirrus cloud inferred from the infrared measurements made by the Moderate Resolution Imaging Spectroradiometer (MODIS). Part I: retrieval method. J Appl Meteorol Climatol 2014;. http://dx.doi.org/10.1175/JAMC-D-13-0215.1 (in press).
[41] Stamnes K, Tsay SC, Wiscombe W, Jayaweera K. Numerically stable algorithm for discrete-ordinate-method radiative transfer in multiple scattering and emitting layered media. Appl Opt 1988;27: 2502–9.
[42] Wan Z, Zhang Y, Zhang Q, Li ZL. Quality assessment and validation of the MODIS global land surface temperature. Int J Remote Sens 2004;25:261–74.
[43] Rienecker M, Suarez M, Todling R, Bacmeister J, Takacs L, Liu H., et al. The GEOS-5 Data Assimilation System – documentation of versions 5.0. 1, 5.1. 0, and 5.2. 0. NASA Tech Rep Series on Global Modeling and Data Assimilation; 2008, vol. 27. p. 1–118.
[44] Tobin DC, Revercomb HE, Moeller CC, Pagano TS. Use of atmospheric infrared sounder high-spectral resolution spectra to assess the calibration of moderate resolution imaging spectroradiometer on EOS Aqua. J Geophys Res 2006;111:D09S5.
[45] Xiong X, Wenny BN, Aisheng W, Barnes WL, Salomonson VV. Aqua MODIS thermal emissive band on-orbit calibration, characterization, and performance. IEEE Trans Geosci Remote Sens 2009;47:803–14.
[46] Brown OB, Minnett PJ, Evans R, Kearns E, Kilpatrick K, Kumar A, et al. MODIS infrared sea surface temperature algorithm theoretical basis document version 2.0. University of Miami; 1999. p. 33149–1098.
[47] Wang W, Liang S, Meyers T. Validating MODIS land surface temperature products using long-term nighttime ground measurements. Remote Sens Environ 2008;112:623–35.
[48] Chen Y. Seasonal surface spectral emissivity derived from Terra MODIS data. In: 13th Conference on Satellite Meteorology and Oceanography; 2004.
[49] Kennedy AD, Dong X, Xi B, Xie S, Zhang Y, Chen J. A Comparison of MERRA and NARR Reanalyses with the DOE ARM SGP data. J Clim 2011;24:4541–57.
[50] McClatchey RA, Fenn R, Selby JA, Volz F, Garing J. Optical properties of the atmosphere. DTIC Document; 1972.
[51] Kahn BH, Liang CK, Eldering A, Gettelman A, Yue Q, Liou KN. Tropical thin cirrus and relative humidity observed by the atmospheric infrared sounder. Atmos Chem Phys 2008;8:1501–18.
[52] Platt CMR. Lidar and radiometric observations of cirrus clouds. J Atmos Sci 1973;30:1191–204.
[53] Bodhaine BA, Wood NB, Dutton EG, Slusser JR. On Rayleigh optical depth calculations. J Atmos Ocean Technol 1999;16:1854–61.
[54] Warren SG, Brandt RE. Optical constants of ice from the ultraviolet to the microwave: a revised compilation. J Geophys Res 2008;113: D14220.
[55] Clough SA, Shephard MW, Mlawer EJ, Delamere JS, Iacono MJ, Cady-Pereira K, et al. Atmospheric radiative transfer modeling: a summary of the AER codes. J Quant Spectrosc Radiat Transfer 2005;91:233–44.
[56] Baum BA, Yang P, Heymsfield AJ, Platnick S, King MD, Hu YX, et al. Bulk scattering properties for the remote sensing of ice clouds. Part II: narrowband models. J Appl Meteorol 2005;44:1896–911.
[57] Miloshevich LM, Heymsfield AJ. A Balloon-borne continuous cloud particle replicator for measuring vertical profiles of cloud microphysical properties: instrument design, performance, and collection efficiency analysis. J Atmos Ocean Technol 1997;14:753–68.
[58] Liu C, Lee Panetta R, Yang P. The effects of surface roughness on the scattering properties of hexagonal columns with sizes from the Rayleigh to the geometric optics regimes. J Quant Spectrosc Radiat Transfer 2013;129:169–85.
[59] Yurkin MA, Hoekstra AG. The discrete-dipole-approximation code ADDA: capabilities and known limitations. J Quant Spectrosc Radiat Transfer 2011;112:2234–47.
[60] Bi L, Yang P, Kattawar GW, Baum BA, Hu YX, Winker DM, et al. Simulation of the color ratio associated with the backscattering of radiation by ice particles at the wavelengths of 0.532 and 1.064 μm. J Geophys Res 2009;114:D00H8.
[61] Yang P, Bi L, Baum BA, Liou K-N, Kattawar GW, Mishchenko MI, et al. Spectrally consistent scattering, absorption, and polarization properties of atmospheric ice crystals at wavelengths from 0.2 to 100 μm. J Atmos Sci 2013;70:330–47.
[62] Hu YX, Winker DM, Vaughan MA, Lin B, Omar A, Trepte C, et al. CALIPSO/CALIOP cloud phase discrimination algorithm. J Atmos Ocean Technol 2009;26:2293–309.
[63] Mace G. Cited. Level 2 GEOPROF product process description and interface control document algorithm version 5.3; 2007 [Available online at ⟨http://www.cloudsat.cira.colostate.edu/dataICDlist.php?go=list&path=/2B-GEOPROF⟩].
[64] Vaughan MA, Powell KA, Winker DM, Hostetler CA, Kuehn RE, Hunt WH, et al. Fully automated detection of cloud and aerosol layers in the CALIPSO lidar measurements. J Atmos Ocean Technol 2009;26: 2034–50.
[65] Chepfer H, Cesana G, Winker D, Getzewich B, Vaughan M, Liu Z. Comparison of two different cloud climatologies derived from CALIOP-attenuated backscattered measurements (Level 1): The CALIPSO-ST and the CALIPSO-GOCCP. J Atmos Ocean Technol 2013;30:725–44.

[66] Sassen K, Wang Z, Liu D. Global distribution of cirrus clouds from CloudSat/Cloud-Aerosol Lidar and Infrared Pathfinder Satellite Observations (CALIPSO) measurements. J Geophys Res 2008;113: D00A12.
[67] King MD, Platnick S, Menzel WP, Ackerman SA, Hubanks PA. Spatial and temporal distribution of clouds observed by MODIS onboard the Terra and Aqua Satellites. IEEE Trans Geosci Remote Sens 2003;41: 459–73.
[68] Rodgers CD. Inverse methods for atmospheric sounding: theory and practice Singapore: World Scientific Publishing; 2000.
[69] Yang P, Gao BC, Baum BA, Wiscombe WJ, Hu YX, Nasiri SL, et al. Sensitivity of cirrus bidirectional reflectance to vertical inhomogeneity of ice crystal habits and size distributions for two Moderate-Resolution Imaging Spectrometer (MODIS) bands. J Geophys Res 2001;106:17267–91.